3-2020

Application of acoustical remote sensing techniques for ecosystem monitoring of a seagrass meadow

Megan S. Ballard
University of Texas at Austin

Kevin M. Lee
University of Texas at Austin

Jason D. Sagers
University of Texas at Austin

Gabriel R. Venegas
University of Texas at Austin

Andrew R. McNeese
University of Texas at Austin

See next page for additional authors

Recommended Citation

Ballard, Megan S., Kevin M. Lee, Jason D. Sagers, Gabriel R. Venegas, Andrew R. McNeese, Preston S. Wilson, and Abdullah F. Rahman. 2020. "Application of Acoustical Remote Sensing Techniques for Ecosystem Monitoring of a Seagrass Meadow." The Journal of the Acoustical Society of America 147 (3): 2002–19. https://doi.org/10.1121/10.0000954

Application of acoustical remote sensing techniques for ecosystem monitoring of a seagrass meadow

Megan S. Ballard, Kevin M. Lee, Jason D. Sagers, Gabriel R. Venegas, Andrew R. McNeese, Preston S. Wilson, and Abdullah F. Rahman

Citation: The Journal of the Acoustical Society of America **147**, 2002 (2020); doi: 10.1121/10.0000954
View online: https://doi.org/10.1121/10.0000954
View Table of Contents: https://asa.scitation.org/toc/jas/147/3
Published by the Acoustical Society of America

JASA ARTICLE

Application of acoustical remote sensing techniques for ecosystem monitoring of a seagrass meadow

Megan S. Ballard,[1,a)] Kevin M. Lee,[1] Jason D. Sagers,[1] Gabriel R. Venegas,[1] Andrew R. McNeese,[1] Preston S. Wilson,[2] and Abdullah F. Rahman[3]

[1]*Applied Research Laboratories, The University of Texas at Austin, Austin, Texas 78713, USA*

[2]*Walker Department of Mechanical Engineering, The University of Texas at Austin, Austin, Texas 78713, USA*

[3]*School of Earth, Environmental, and Marine Science, The University of Texas Rio Grande Valley, Brownsville, Texas 78520, USA*

ABSTRACT:

Seagrasses provide a multitude of ecosystem services and serve as important organic carbon stores. However, seagrass habitats are declining worldwide, threatened by global climate change and regional shifts in water quality. Acoustical methods have been applied to assess changes in oxygen production of seagrass meadows since sound propagation is sensitive to the presence of bubbles, which exist both within the plant tissue and freely floating the water as byproducts of photosynthesis. This work applies acoustic remote sensing techniques to characterize two different regions of a seagrass meadow: a densely vegetated meadow of *Thalassia testudinum* and a sandy region sparsely populated by isolated stands of *T. testudinum*. A Bayesian approach is applied to estimate the posterior probability distributions of the unknown model parameters. The sensitivity of sound to the void fraction of gas present in the seagrass meadow was established by the narrow marginal probability distributions that provided distinct estimates of the void fraction between the two sites. The absolute values of the estimated void fractions are biased by limitations in the forward model, which does not capture the full complexity of the seagrass environment. Nevertheless, the results demonstrate the potential use of acoustical methods to remotely sense seagrass health and density. © *2020 Acoustical Society of America*. https://doi.org/10.1121/10.0000954

(Received 19 December 2019; revised 6 March 2020; accepted 6 March 2020; published online 30 March 2020)

[Editor: John A. Colosi] Pages: 2002–2019

I. INTRODUCTION

Seagrasses provide a multitude of ecosystem services: they alter water flow, cycle nutrients, stabilize sediments, support food web structure, and provide a critical habitat for many animals (Orth *et al.*, 2006). Additionally, seagrasses serve as important organic carbon stores; they contribute up to 15% of global ocean carbon sequestration (Fourqurean *et al.*, 2012). However, seagrass habitats are declining globally, losing 7% of their known area per year (Waycott *et al.*, 2009). Threats to seagrass meadows and their associated ecosystems include global climate change (increases in sea surface temperature, sea level, and frequency and intensity of storms), regional shifts in water quality, and localized impacts due to increased loading of sediment, contaminants, and nutrients (Orth *et al.*, 2006).

Dissolved oxygen measurements made with chemical sensors are the most widely used method for measuring oxygen production in seagrass plants and are among the most important parameters to measure as indicators of seagrass meadow productivity (Silva *et al.*, 2009). However, when the oxygen level in the water is saturated, free gas bubbles exist in the water that are not measured by chemical sensors. Since oxygen saturation is the normal condition in seagrass meadows, measurements of dissolved oxygen are only accurate under low light conditions such as the early morning hours (Long *et al.*, 2019; Wilson *et al.*, 2012). On the other hand, sound propagation is very sensitive to the presence of bubbles, and acoustic methods have been used to assess changes in oxygen production of seagrass meadows with high temporal resolution (Chang *et al.*, 2019; Felisberto *et al.*, 2015; Hermand, 2004; Hermand *et al.*, 1998; Lee *et al.*, 2019).

Acoustic inference techniques have been proven as effective and reliable in determining physical properties of the upper sediments in littoral environments (Chapman *et al.*, 2003; Dettmer *et al.*, 2010; Dosso and Nielsen, 2002b; Hermand, 1999; Holland and Osler, 2000) and as well as in very shallow constrained environments (Ballard *et al.*, 2018a). In this work, these methods are applied to determine the volume fraction of gas present in two different regions of a seagrass meadow where the average water depth was approximately 1 m. The acoustic measurements were collected in a densely vegetated meadow of *Thalassia testudinum* and in a sandy region sparsely populated by isolated stands of *T. testudinum*. The acoustic data recordings of broadband signals from a Combustive Sound Source (CSS) are distinct between the two sites. Bayesian methods, as well as an approximate analytic approach, are applied to estimate the void fraction, defined as the fraction of the volume of gas over the total volume. The void fraction is valued between 0, for no gas present, and 1, for only gas

[a)]Electronic mail: meganb@arlut.utexas.edu

 0001-4966/2020/147(3)/2002/18/$30.00

https://doi.org/10.1121/10.0000954

present. The methods are applied to acoustic data collected at the two sites, and the results reflect the relative productivity of the seagrass in the two environments.

The use of acoustical methods to monitor seagrass productivity was first proposed by Hermand *et al.* (2000). This pioneering work used forward modeling to provide evidence that the inverse problem of determining the void fraction of gas within the seagrass meadow could be solved. The work presented in this paper represents the first application of inference techniques to estimate the void fraction of gas present in the seagrass meadow from a set of acoustic measurements. The results were obtained through the novel application an effective medium model capable of predicting the frequency-dependent sound speed and attenuation over a wide frequency band. The modeling approach is based on spherically shaped bubbles freely floating a liquid, and it does not account for complexities of gas bubbles constrained by plant tissue such as the gas cavity shape and the elasticity and structure of the leaves, roots, and rhizomes. Neglecting these factors biases the results, but the comparisons between the void fractions estimated for the densely and sparsely vegetated sites are convincing. Additionally, the acoustic data reported in this manuscript display exceptional propagation effects related to the very shallow water depths at the experiment sites. The ability to track the modal cut-off frequency, which is inversely proportional to water depth, is exploited to form an analytical relationship between the spectra of the measured signals and the void fraction of gas in the seagrass meadow. Furthermore, the evaluation of two sites with varying densities of seagrass provides a rare opportunity to compare results from the acoustic methods.

A. Thalassia testudinum

Seagrasses are marine flowering plants found in shallow bays, estuaries, and coastal waters. The depth at which seagrass is found is limited by water clarity, which determines the amount of light reaching the plant. Chloroplasts in seagrass tissues use the sun's energy to convert carbon dioxide and water into sugar and oxygen for growth through the process of photosynthesis. Gas bodies within the seagrass tissue, known as lacunae, exchange oxygen and carbon dioxide throughout the plant and help keep the leaves buoyant. Seagrass leaves have a thin cuticle layer, which allows gasses and nutrients to diffuse directly into and out of the leaves from the water. The roots and rhizomes of seagrasses extend into the sediment and are used to store and absorb nutrients. Under high irradiance, the partial pressure of oxygen contained in the lacunae can exceed that of the surrounding water, and oxygen diffuses through the plant tissue to form bubbles on the surfaces of the leaves. Oxygen is also transferred through the roots and rhizomes to the surrounding sediment due to generally hypoxic conditions.

Thalassia testudinum, also known as turtlegrass, is a species of seagrass commonly found in the lower regions of Texas along mud-sand bottoms in water depths of 0.5–1.5 m. *T. testudinum* was the dominant species within the lagoon studied in this work. It derives its common name from the fact that it is a favorite food source for the green sea turtle. *T. testudinum* grows from a long, jointed rhizome that is found from 5 to 10 cm below the seafloor. Seagrass leaves form within individual shoots, bundled in thin protective sheaths that grow vertically upwards from nodes in the rhizome. The leaf blades are 2 cm wide with rounded apical ends and grow to 30 cm in height. Epiphytes grow on the grasses, and algae, diatoms, and bacterial films can cover the surface of the leaf blades.

To characterize the lacunae contained within the seagrass tissue, Computed Tomography (CT) imagery of the seagrass blades and sediment containing roots and rhizome were acquired using the High-Resolution X-ray CT Facility of the University of Texas at Austin. These new measurements build on previous works, which used CT imagery (Wilson *et al.*, 2010) as well as microscopic cross-sections (Wilson and Dunton, 2009) to estimate the gas volume present in *T. testudinum* tissue. The estimated gas volumes were used to inform effective medium models to predict the sound speed of water containing seagrass leaf blades and/or rhizomes for comparison with laboratory-based experiments. The high resolution measurements of the seagrass leaves, roots, and rhizomes provided in this work are suitable for determining the shapes of the gas cavities present throughout the plant. A more rigorous determination of size distribution and overall volume fraction of the lacunae is left to future work.

To image the seagrass leaf blade, the blade was rolled into a coil with the apical end positioned on the inside of the coil. The coil was then scanned at a resolution of 10.6 μm and the 8-bit grayscale imagery was processed by thresholding the range of grayscale values of the seagrass tissue and entrained gas. A cross-section of the coil showing the seagrass tissue (green) and lacunae (blue) is shown in Fig. 1(a). The lacunae form a series of long, narrow, segmented channels that extend from the basal end (exterior of the coil) to the apical end (interior of the coil) of the leaf blade. Wider channels are observed near the basal end of the leaf. Over the length of the leaf (i.e., all cross sections) wider channels are found near the center of the blade, with narrow channels on the outside edges. The gas channels in the outer coil are shown in Fig. 1(c), and the presence of thin membranes segmenting the channels observable as perforations in the lacunae.

An image obtained from the sediment bearing a seagrass sheath and roots is displayed in Fig. 1(b). Because the sediment core represented a larger volume of material, the scan was acquired at a lower resolution of 38.1 μm. Following the same procedure described for the leaf blade, the image was created by thresholding the densities of the different components which, for this case, included the sediment, shells, seagrass tissue, and entrained and free gas. The sediment contained significant quantities of shell and shell hash, which are not shown in Fig. 1(b), so that the seagrass tissue and lacunae can be clearly observed. A sheath can be

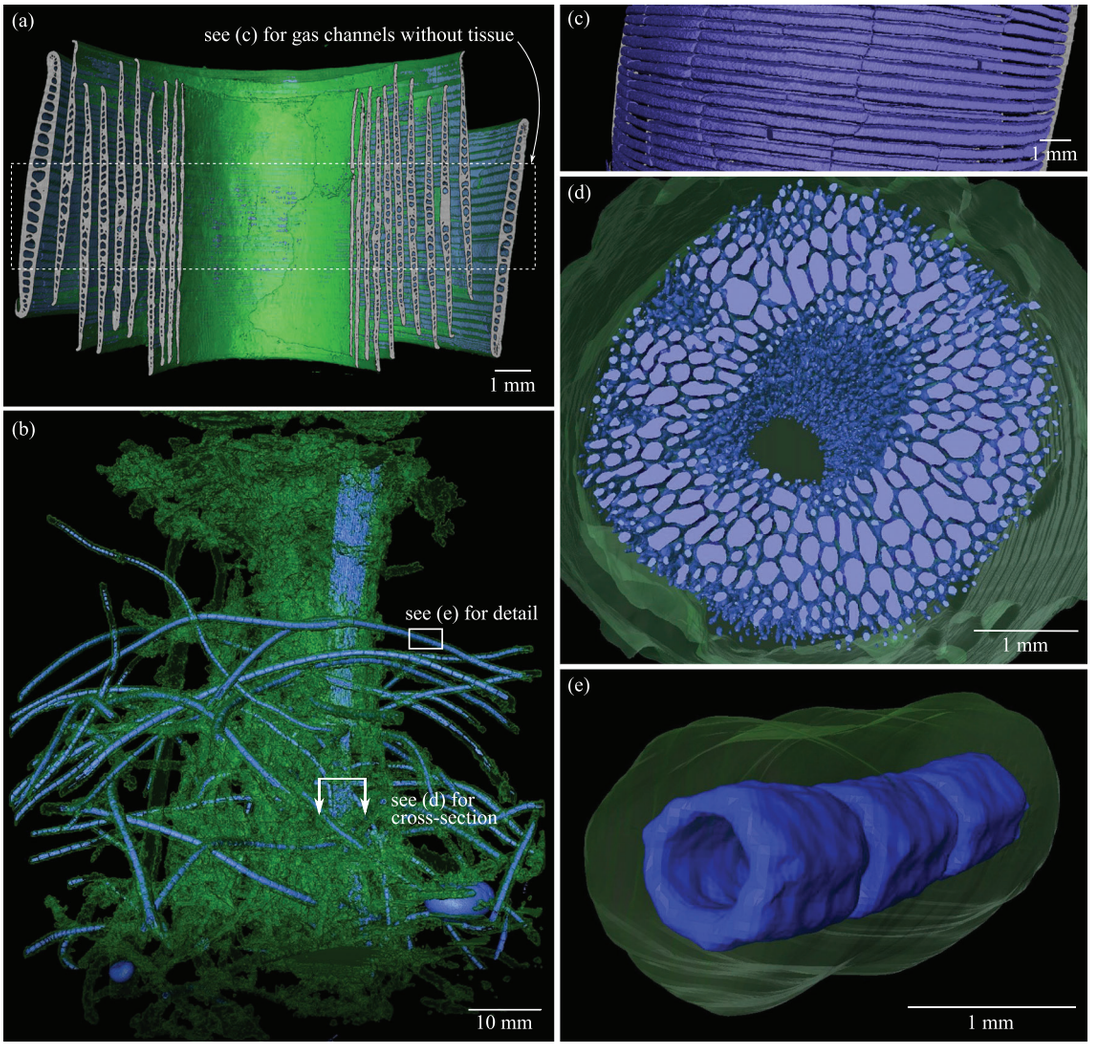

FIG. 1. (Color online) (a) CT image of a seagrass blade, which was curled around itself with apical end of the leaf positioned on the inside of the coil. The seagrass tissue is shown in translucent green, the lacunae are shown in blue, and the cross-section of the blade are shown in gray. (b) CT imagery of the upper 10 cm of a 7.6 cm diameter sediment core containing the vertically orientated sheath and horizontally orientated roots. The seagrass tissue is shown in translucent green, the lacunae and free gas bubbles are shown in blue. (c) Gas channels in the outer coil of the seagrass blades, tissue not shown. (d) Cross-section showing the gas volumes contained in the vertically-orientated rhizome. (e) Detailed view of the segmented tubular gas cavities in the roots.

seen vertically orientated in the center core. It is composed of densely-packed, small gas cavities embedded in the seagrass tissue, which can be observed in the cross-sectional view shown in Fig. 1(d). A thick matte of seagrass roots is primary horizontally orientated throughout the sediment core. The roots each contain a train of non-intersecting segmented tubular gas cavities. Their shape can be studied in the detailed view showing three gas cavities in Fig. 1(e). Finally, a few bubbles trapped in the sediment can also be observed near the bottom of the core section.

B. Effective medium models for bubbly liquids

Techniques exist to calculate acoustic propagation through the complex geometry of gas cavities encapsulated in seagrass tissue. Applications of the finite element method to bubbles encapsulated within human tissue provide examples of the analogous modeling capability (Nightingale *et al.*, 2000; Song *et al.*, 2016). However, these approaches are extremely computationally intensive and are generally limited to small physical domains making them unsuitable for calculating acoustic propagation at the scale of a seagrass meadow. Furthermore, the statistical inference method employed in this work requires tens of thousands of iterations of forward model runs to achieve convergence. Therefore, a computationally efficient modeling approach is required. This work utilizes an effective medium model that applies a suitably chosen average to the microscopic conservation laws and introduces averaged field variables. The resulting averaged governing equations replace the complex distribution of scatterers within a host medium with a continuous effective medium (Commander and Prosperetti, 1989). This approach neglects the effects of seagrass tissue which have a damping effect on the acoustic response to gas

https://doi.org/10.1121/10.0000954

cavities (Church, 1995). Nevertheless, the application of an effective medium model provides an efficient means to estimate the volume of gas present within the seagrass meadow, and the use of this approach is consistent with previous assessments (Ballard *et al.*, 2018b; Hermand *et al.*, 2000; Wilson *et al.*, 2010; Wilson and Dunton, 2009).

A mathematical model for the propagation of acoustic waves in a bubbly liquid (Commander and Prosperetti, 1989), which is applied in this work to calculate acoustic propagation through the seagrass meadow, is briefly described here. Given a void fraction of gas present in the liquid and distribution of spherical bubble sizes, a frequency-dependent effective sound speed and attenuation are calculated from the wavenumber k_m,

$$k_m^2 = k^2 + 4\pi\omega^2 \int_0^\infty \frac{f(a)ada}{\omega_0^2 - \omega^2 + 2i\omega(b_v + b_t + b_a)}, \tag{1}$$

where a is the bubble radius and $i = \sqrt{-1}$. The wavenumber for the bubble-free liquid is given by $k = \omega/c_l$, where ω is the angular frequency and c_l is the sound speed in the bubble-free liquid. The bubble resonance frequency $f_0 = \omega_0/2\pi$ is calculated according to

$$\omega_0^2 = \frac{1}{\rho_l a^2}\left[3\kappa p_0 - \frac{2\sigma_b}{a}\right], \tag{2}$$

where ρ_l is the liquid density, p_0 is the equilibrium pressure inside the bubble, and σ_b is the liquid surface tension. The viscous, thermal, and acoustic loss terms (b_v, b_t, and b_a, respectively) each account for different mechanisms of energy dissipation due to the presence of bubbles

$$b_v = \frac{2\mu_l}{\rho_l a^2}, \tag{3}$$

$$b_t = \frac{2\mu_{th}}{\rho_l a^2}, \tag{4}$$

$$b_a = \frac{\omega k a}{2}. \tag{5}$$

The polytropic exponent of gas inside the bubble present in Eq. (2) and the viscosity-like term in Eq. (4) are given by

$$\kappa = (1/3)\mathrm{Re}(\Phi) \tag{6}$$

and

$$\mu_{th} = \frac{p_0}{4\omega}\mathrm{Im}(\Phi), \tag{7}$$

where Φ is given by Eq. (41) of Prosperetti *et al.* (1988) as a function of the frequency, bubble radius, ratio of specific heats, and the gas thermal diffusivity. The integral in Eq. (1) is over an arbitrary bubble size distribution $f(a)$.

In this application, a Gaussian bubble size distribution $f(a)$ was assumed

$$f(a) = \frac{C}{\sigma_0\sqrt{2\pi}} e^{-(a-a_0)^2/(2\sigma_0^2)}, \tag{8}$$

where σ_0^2 is the variance, a_0 is the mean bubble radius, and C is a scaling parameter that relates the bubble size distribution to the volume fraction.

The frequency-dependent phase speed V and attenuation α are computed by

$$V = \frac{\omega}{\mathrm{Re}(k_m)} \tag{9}$$

and

$$\alpha = \mathrm{Im}(k_m). \tag{10}$$

For frequencies sufficiently well below the individual bubble resonance frequency f_0, the effective sound speed can be approximated by the Mallock-Wood equation (Mallock, 1910; Wood, 1946), which is frequency independent and is given by

$$c_{MW} = c_l\left[\left(1 + \left(\frac{\rho_g}{\rho_l} - 1\right)(1-\beta)\right) \times \left(1 - \left(1 - \frac{B_l}{B_g}\right)(1-\beta)\right)\right]^{-1/2}, \tag{11}$$

where ρ_g is the density of the gas inside the bubble, B_g and B_l are the bulk moduli of the gas and liquid phases, and β is the void fraction of gas present in the water. At sufficiently low frequencies, Eqs. (1) and (11) approximately yield the same sound speed.

C. Acoustic sensing of photosynthesis

Initial work on acoustic sensing of photosynthesis by seagrass was conducted by Hermand (Hermand, 2004; Hermand *et al.*, 1998, 2000). His work concentrated on *Posidonia oceanica*, a Mediterranean species of seagrass with a thick matte consisting of interlaced remnants of roots, rhizomes, and entangled sediment. In his original experiment (Hermand *et al.*, 2000), the water depth was 25 m and the seagrass meadow was modeled as a set of layers, the first being near the bottom of the water column and representing the leaves, and the second layer being in the upper sediments and representing the rhizome matte. By varying the effective sound speed, as determined by the Mallock-Wood equation [Eq. (11)], between 500 and 1500 m/s within the seagrass layer, Hermand demonstrated that the low-order modes could become trapped within the seagrass layer during periods of increased photosynthetic activity in a manner consistent with the measurements. Modeling results showed that mode 1 became trapped in the seagrass layer for void fractions between 5×10^{-6} and 4×10^{-5} over the entire frequency band (from 0.1 and 1.6 kHz), and mode 2 became trapped in the seagrass layer for void fractions of 1×10^{-4} for the higher portion of the frequency band (from 0.8 to

1.6 kHz). These results were reinforced by a later experiment which involved a lower density *P. oceanica* bed that had much lower oxygen productivity and smaller diurnal acoustic fluctuations (Hermand, 2006).

More recent experimental work by Felisberto *et al.* (2015) built on Hermand's earlier work using an autonomous experiment deployed in a *P. oceanica* meadow with an average water depth of 38 m. The measurements were collected in three frequency bands spanning from 0.4 to 8.5 kHz, and they demonstrated a high degree of correlation between the diurnal changes in the received acoustic energy and in the estimated water column oxygen bubble concentration, which was derived from dissolved oxygen measurements. Motivated by previous work which showed a linear relationship between gases discharged from the aerenchyma and oxygen released into the water column (Roberts and Caperon, 1986), they developed an empirical relationship between perturbations in the acoustic energy and perturbations in the dissolved oxygen. However, such a relationship does not account for the effects of the gas entrained within the seagrass tissue and other characteristics of the waveguide (water column sound speed profile, sediment properties, etc.) which also contribute to acoustic losses making it necessary to recalibrate this relationship for each environment.

In contrast to the *P. oceanica* experiments described above, which involved moderate water depths (>8 m) and propagation distances (>53 m), an acoustic data set recorded in a very shallow (<1 m) meadow of *Cymodocea rotundata* over considerably shorter distances (<6 m) showed even more extreme diurnal effects (Chang *et al.*, 2019). Over a 24-h period, the mean spectral level of the acoustic signals varied by 57 dB in the 4–5 kHz frequency band. By examining the relative loss in different portions of the frequency band, a resonant bubble radius of 0.4–0.8 mm was determined and corroborated with video footage of the seagrass bubbles. Numerical modeling of a seagrass-free waveguide showed that the tidal and temperature variations contributed to 13 dB in acoustic variability, and the excess variation in the received level was attributed to the acoustical effects of bubbles due to oxygen released by the photosynthetic processes of the seagrass. However, the modeling neglected to consider the percentage of the waveguide which was filled by the seagrass canopy during different parts of the tidal cycle which caused variations in the water depth from 0.3 to 0.84 m. Modeling which includes the acoustical effects of the bubbles is needed to more conclusively disentangle the variations in received level to that of seagrass versus other environmental factors.

Using a similar experimental set up to that of Chang *et al.* (2019), a complementary set of short-range measurements (Lee *et al.*, 2019) was collected simultaneously to the data set presented in this paper. These short-range data were collected in the Lower Laguna Madre in the same locations as the long-range data presented in this paper. For both measurements, the average water depth was close to 1 m and the seagrass canopy, which was composed primarily of *T. testudinum*, filled a significant portion of the water column. The measurements were collected over a wider frequency band (from 0.1 to 100 kHz) than the previous works, which allowed for identification of an excess attenuation band that occurred from 3.5 to 35 kHz in the afternoon when bubble production from photosynthesis was at a maximum. From an examination of the frequency dependence of the acoustic loss, an average resonant bubble radius of 0.35 mm was estimated. For frequencies below 2.5 kHz, no discernible diurnal changes in the received signal level were observed. These short-range, broadband measurements were also collected in a nearby sparsely vegetated site, for which the received signal level was higher than that of the densely vegetated site by 25 dB in terms of spectral level averaged over the entire frequency band. These observations led to the hypothesis that bubbles within the seagrass tissue were primarily responsible for the difference in low-frequency acoustic propagation effects between the sparsely and densely vegetated sites.

Finally, a preliminary experiment conducted in a nearby location within the Lower Laguna Madre provided data suitable for geoacoustic inference (Ballard *et al.*, 2018b). The results were sensitive to the presence of bubbles in the water layer as determined from the narrow shape of the cost function envelope. The void fraction of gas bubbles was estimated as 2.18×10^{-4}. This value is notably higher than Hermand's estimates, but these data were acquired in a different type of seagrass during the peak growth season in July. A comparison of modeled time series data using the estimated void fraction to modeled time series data using a negligible void fraction showed that the seagrass bubbles had the effect of attenuating the peak spectral level by 30 dB and reducing the frequency of the spectral peak by a factor of five.

II. METHODS AND MATERIALS

The experiment was conducted in the Lower Laguna Madre during 3–4 October 2018. The Laguna Madre is a long, shallow, hypersaline lagoon located between the mainland of South Texas and Padre Island. *T. testudinum* is the dominant species within the lagoon, although small stands of *Halodule wrightii* and *Syringodium filiforme* occur locally (Kaldy and Dunton, 2000). The seagrasses of the Lower Laguna Madre are representative of the Tropical Atlantic bioregion, which includes the Gulf of Mexico and the Caribbean Sea (Short *et al.*, 2007). In early October, *T. testudinum* is typically just past the annual peak of its above-ground biomass (Kaldy and Dunton, 2000).

Data were collected at two sites located on the eastern side of the lagoon as shown in Fig. 2(a). The motivation in choosing these two sites was to have a seagrass site completely covered by a homogenous meadow of *T. testudinum*, and a seagrass-free site completely devoid of seagrass. Ideally, the seagrass-free site would provide a control experiment designed to minimize the effects of variables (i.e., water depth, sediment type, water column variability, surface roughness) other than the independent variable (i.e., seagrass). Such an experiment

JASA
https://doi.org/10.1121/10.0000954

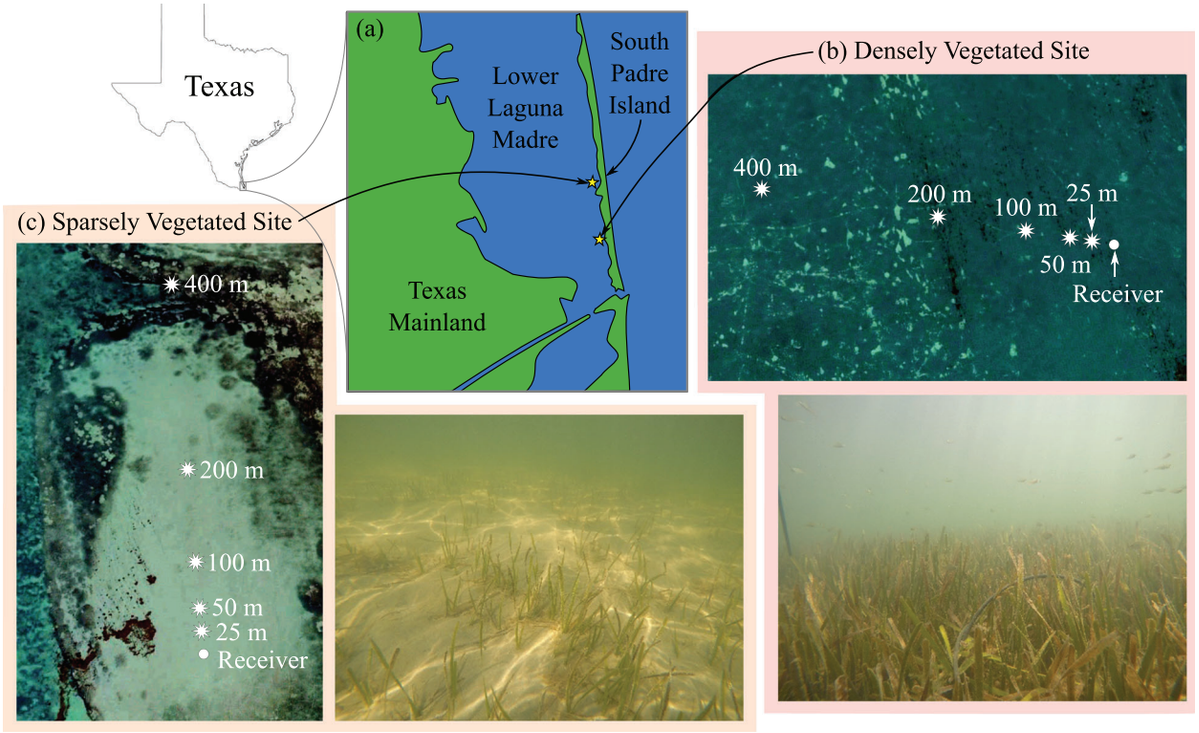

FIG. 2. (Color online) (a) Map of the Lower Laguna Madre with the locations of experiment sites indicated by stars. (b) Satellite imagery of the densely vegetated site with the location of the hydrophone receiver (circle) and source locations (stars), and a photograph of the seagrass coverage. (c) Satellite imagery of the sparsely vegetated site with the location of the hydrophone receiver (circle) and source locations (stars), and a photograph of the seagrass coverage.

design can increase the reliability of the results, often through a comparison between control measurements and the other measurements. However, such exemplary sites were not realized in the natural environment, and the experiment sites are approximations of these ideals.

The first site, located at 26° 06′ 20.5″ N, 97° 10′ 30.4″ W, was covered by a dense meadow of seagrass interspersed with barren patches having length scales ranging from tens of centimeters to tens of meters. These barren patches can be observed as light areas in the satellite imagery shown in Fig. 2(b). Barren patches can result from natural causes including erosion from storms and currents (Allaoui *et al.*, 2016), or from anthropogenic causes such as anchoring and propeller scars (Dunton and Schonberg, 2002). Inhomogeneities along the propagation paths are noted, with the west end of the path appearing to have more barren patches than the region around the receiver. The water depth at this site ranged from approximately 0.9 to 1.4 m depending on the tide. A representative photograph of the seagrass canopy is shown in Fig. 2(b). Numerous fish, as well as the hydrophone cable, can also be seen in the photo.

The sparsely vegetated site was located at 26° 09′ 03.2″ N, 97° 11′03.8″ W, approximately 5 km north of the densely vegetated site. The sparsely vegetated site was chosen for its similar characteristics to the densely vegetated site in terms of water depth, geographic location, and ambient conditions. As shown in the photograph, the lagoon floor was sandy and sparsely populated by isolated stands of seagrass. This thin seagrass coverage is representative of the majority of the propagation paths. However, as shown by the satellite imagery in Fig. 2(c), the location of the 400 m source was different. The average water depth was 0.8 m, which is slightly shallower than the densely vegetated site.

For both the densely and sparsely vegetated sites, acoustic data recordings of broadband signals from a CSS were recorded on a bottom-mounted hydrophone, deployed from an anchored monitoring boat. The CSS was deployed from a second boat along a transect at positions 25, 50, 100, 200, and 400 m away from the hydrophone. At each CSS position, a minimum of three CSS transects was recorded at each position. For the densely vegetated site, which was targeted as the primary interest for this work, the CSS signals were recorded at five separate times throughout the day on 3 October 2018. At the less vegetated site, one transect was conducted, with the measurements occurring mid-morning on 4 October 2018. The times of the data collections at both sites are listed in Table I.

TABLE I. Experiment time table. Times are given in local time.

Site and transect	date	Start time	End time
DVS Transect 1	3 October	6:54	8:12
DVS Transect 2	3 October	9:27	10:27
DVS Transect 3	3 October	12:05	13:10
DVS Transect 4	3 October	14:08	14:55
DVS Transect 5	3 October	15:49	16:21
SVS Transect 1	4 October	10:11	11:34

A. Supporting environmental measurements

During the experiment, environmental parameters including solar irradiance, dissolved oxygen, water temperature, and water depth were measured at the receiver location at each of the experiment sites. Wind speed and wind direction were obtained from NOAA weather buoy 877948 located at 26° 4′ 21″ N, 97° 10′ 1″ W, about 3.7 km south of the densely vegetated site. These data are shown in Fig. 3, with the filled circles showing measurements pertaining to the densely vegetated site recorded on 3 October 2018, and the open circles showing measurements pertaining to the sparsely vegetated site recorded on 4 October 2018. Since the measurements of solar irradiance, dissolved oxygen, water temperature, and water depth were only acquired when the acoustic experiment was taking place, the measurements on 4 October 2018 span a shorter time period. The shaded areas represent the periods of the acoustic measurements.

Measurements of solar irradiance were obtained using a pyranometer mounted on the stationary boat monitoring the hydrophone receivers. As shown in Fig. 3(a), solar irradiance begins to increase just before 8:00 on 3 October 2018.

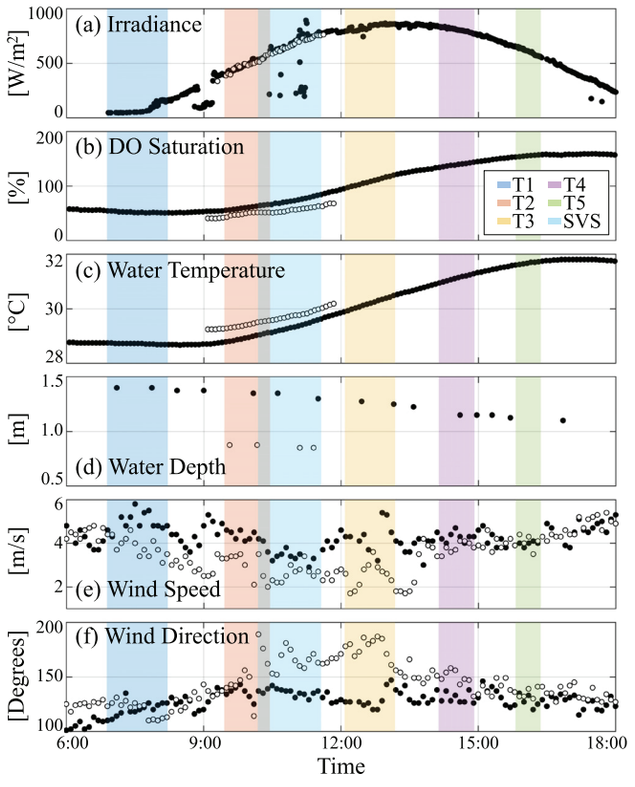

FIG. 3. (Color online) Environmental parameters measured (a)–(d) at the experiment sites and by a (e)–(f) NOAA weather buoy. In all plots, the data recorded at the densely vegetated site on October 3 are shown by the solid circles, and data recorded at the sparsely vegetated site on October 4 are shown by the open circles. The shaded areas represent the time periods during which the acoustic measurements were recorded. The horizontal axis is local time on October 3 for the measurements at the densely vegetated sites (listed as T1–T5 in the legend) and local time on October 4 for the measurements at the sparsely vegetated site (listed as SVS in the legend).

It increased until reaching a maximum level around 13:00, after which solar irradiance decreased. Local minima are observed at several times throughout the day when clouds passed overhead and blocked the direct sunlight. The solar irradiance data measured 4 October 2018 between 9:30 and 11:30 at the sparsely vegetated site were nearly identical to the data recorded at the densely vegetated site.

Measurements of dissolved oxygen and water temperature were obtained with a probe submerged near the lagoon floor. As shown in Figs. 3(b) and 3(c), both quantities are observed to increase during the course of the day, with a time lag relative to the solar irradiation of approximately three to four hours. In comparing the densely and sparsely vegetated sites, it is observed that the sparsely vegetated site is characterized by a lower level of dissolved oxygen that increased more slowly [see Fig. 3(b)]. The presumed reason for this difference is the lower amount of seagrass present at the sparsely vegetated site. Additionally, the water temperature was approximately 0.5 °C warmer at the sparsely vegetated site [see Fig. 3(c)].

Water depth was measured at the receiver positions using a marked rod. The tidal effects are evident in the measurements from 3 October 2018, and the water depth is observed to decrease over the course of the measurement period [see Fig. 3(d)]. Water depth was also measured at the CSS positions, and the variation in depth along the propagation path was within 10 cm of the depth recorded in Fig. 3(d). The water depth at the less vegetated site was approximately 0.5 m shallower than that of the densely vegetated site at the same time of day.

Wind direction and wind speed data from NOAA buoy 8779748 were obtained from the National Oceanic and Atmospheric Administration (National Buoy Data Center, 2019). During the times of both densely vegetated site (DVS) and sparsely vegetated site (SVS) experiments, the wind speeds were low (less than 6 m/s), displaying little dependence on time of day, and no breaking waves were observed. The wind came primarily from the east-southeast on 3 October 2018, and averaged a southerly direction during the measurement period on 4 October 2018.

B. CSS

The CSS produces a repeatable, broadband signal with peak frequency components below 100 Hz (McNeese *et al.*, 2010, 2012; Wilson *et al.*, 1995). The CSS is comprised of three main components: a submersible combustion chamber, a gas delivery system, and an ignition system. This work utilized a small combustion chamber constructed from a 4-inch National Pipe Thread (NPT) pipe nipple 15.2 cm in length (McNeese *et al.*, 2012). The chamber was lowered to mid-depth in the water column, about 0.5 m below the surface, and then the chamber was filled with a stoichiometric ratio of hydrogen and oxygen gas. The gas was then ignited by a spark plug positioned in the top of the chamber, causing the gas to turn into high temperature combustion products (mostly water vapor). The resulting bubble motion radiates

https://doi.org/10.1121/10.0000954

acoustic pulses. First, a positive pressure pulse is radiated right after the completion of the combustion process. Next, a broad negative-going pulse occurs as the bubble grows. This is followed by a strong, sharp positive pulse, which occurs upon bubble collapse and vapor condensation. Finally, a few smaller bubble oscillations occur as the rest of the vapor condenses.

The CSS was deployed from a second small boat, as the first boat was occupied with recording the signals from the hydrophones and acquiring the environmental measurements. The acoustic pressure signals radiated by the CSS were recorded by a reference hydrophone, located approximately 1 m from the combustion chamber. Because the combustion chamber was located near the waveguide boundaries, the reference signal was contaminated by reflections from the sea surface and the estuarine floor as well as reflections from the hull of the boat. An additional impediment of the monitor hydrophone measurements was the 40 kHz sampling rate may have been insufficient to capture the peak pressure of the bubble collapse due to the fast rise time of the resultant acoustic impulse.

To reconstruct the source waveform for use in subsequent data interpretation and propagation modeling, the CSS signals were modeled as a train of Gaussian pulses. An example of a measured and reconstructed source waveform recorded at the sparsely vegetated site is shown in Fig. 4. The beginning of the time series shows the small initial pulse associated with the combustion process. The peak pressure is observed at 0 ms when the displaced water collapses back into the chamber. The subsequent pulses result from oscillations of the residual combustion products in the chamber.

The measured waveform includes contributions from surface and bottom reflections, which result in the reduced amplitude of the bubble collapse and the subsequent fluctuations [see the inset figure in Fig. 4(a)]. In the reconstructed waveform, the Gaussian pulses have fixed amplitudes and variance, but the mean is aligned to the arrival times of the bubble collapse and bubble oscillations of the individual CSS signals. Although the amplitudes were fixed in the definition of the reconstruction, source amplitude was included as an unknown parameter in the geoacoustic inference. The spectra of the measured and reconstructed source waveforms are shown in Fig. 4(b). There is good agreement in the frequency spectra, especially between 100 Hz and 1 kHz where the majority of the energy of the propagated signal is received. The dip in the spectra of the measured signal near 1.5 kHz is attributed to the waveguide propagation effects.

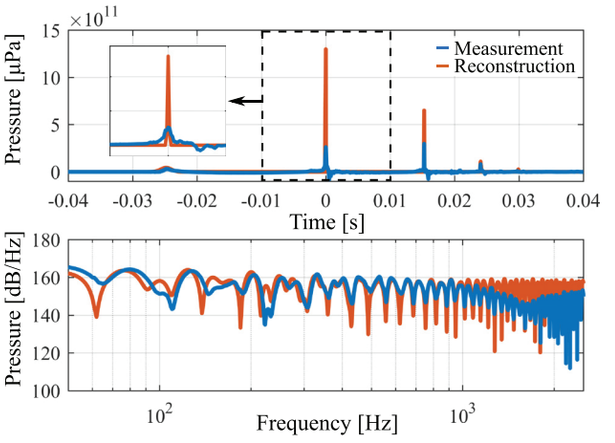

FIG. 4. (Color online) (a) Measured and reconstructed source waveforms recorded at the sparsely vegetated site. Inset figure shows a closeup of the bubble collapse. (b) Spectra of the measured and reconstructed source waveforms.

C. Acoustic measurements

The downrange CSS signals were measured using a High Tech Inc. dual sensitivity HTI-90-U hydrophone mounted a few centimeters above the seafloor by attaching the hydrophone to a 60 cm section of reinforcing bar (rebar). The free end of the rebar was inserted into the seafloor to secure the hydrophone's position. The hydrophone was cabled back to the boat, where the signals were conditioned, digitized at a sampling rate of 40 kHz, and stored on a computer. The sensitivity of the hydrophone and gain of the recording system were adjusted at required times along the transect to maximize the dynamic range of the measured signals (see Table II). This was necessary because the peak pressure of the CSS signals varied from 177 dB re 1 μPa at the nearest CSS position to 137 dB re 1 μPa at the most distant.

Measured time series at densely and sparely vegetated sites are shown in Fig. 5. For the densely vegetated site, waveforms from Transect 2 were used for the comparison since they were measured close to the same time of day as the single set of measurements acquired at the sparsely vegetated site. In the plots, the vertical axis represents the distance from source to receiver, and it is shown on a logarithmic scale. The received signals are multiplied by the source/receiver separation distance so that their relative amplitudes can be compared. Since the signal amplitudes still decay with range, this indicates they have undergone loss that exceeds spherical spreading. Within each signal, it is possible to observe the arrival of the bubble growth, bubble collapse, and bubble oscillations. These features can most readily be seen in the waveform recorded at 100 m range in the sparsely vegetated site.

In both plots, the black dashed line represents a linear fit to the arrival time of the onset of the received signals. It appears curved because of the logarithmic scaling of the vertical axis. The slopes of the lines are 1758 and 1653 m/s for

TABLE II. Hydrophone sensitivity and gain.

Range	Sensitivity (dB)	Gain (dB)
25 m	−220	40
50 m	−220	40
100 m	−168	0
200 m	−168	0
400 m	−168	20

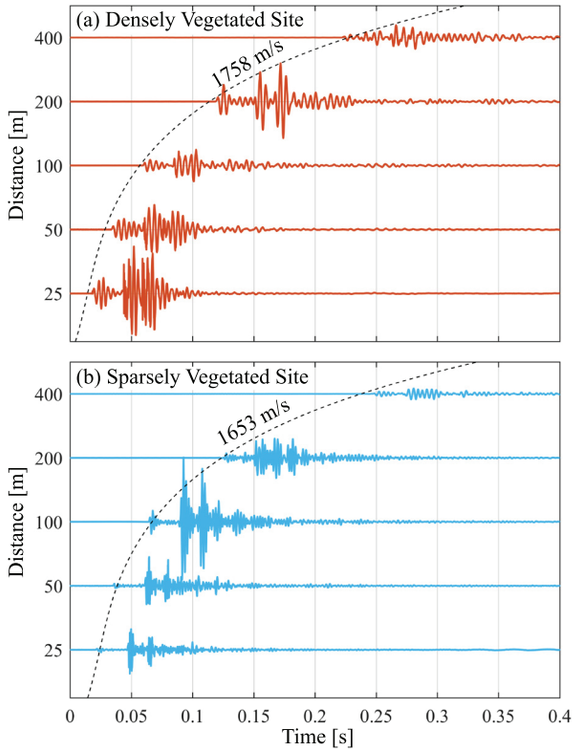

FIG. 5. (Color online) Measured time series recorded at the (a) densely vegetated site (Transect 2) and (b) sparely vegetated site. In both plots, the y axis is distance from source to receiver and is shown on a logarithmic scale. The received signals are multiplied by the source/receiver distance so their relative amplitudes can be compared. The dashed black line is a linear fit to the arrival of the signals, and the estimated wave speeds are listed near the curves.

the densely and sparsely vegetated sites, respectively. Both of these values are considerably greater than the measured water column sound speed of 1542 m/s, and these estimated speeds are characteristic of a ground wave propagation in a Pekeris waveguide. For this case, the arrival time t is calculated according to $t = r/c_b$ where r is the propagation range and c_b is the sound speed in the bottom (Choi and Dahl, 2006). Thus, the estimated wave speeds are assumed to be that of the sediment and not the water column.

Comparing the signals recorded at the densely and sparsely vegetated sites, it is observed that the sparsely vegetated site has more high frequency content. The higher frequency components of the signal have been attenuated at the densely vegetated site. Additionally, because the sparsely vegetated site lacks significant low frequency content, the amplitudes of the measured waveforms are roughly equivalent at both sites.

Within a single site, there are some deviations to the expected trend of decreasing amplitude with increasing source range. Notably, the received level at the 100 m CSS location at the densely vegetated site [see Fig. 5(a)] appears lower than the surrounding measurements, and the received level at the 100 m CSS location at the sparsely vegetated site [see Fig. 5(b)] appears higher than the surrounding measurements. These outliers are attributed to inhomogeneities in the lagoon bed that facilitate better or poorer source coupling with the bottom for propagation of the ground wave.

The frequency spectra for the measured signals at both the densely and sparsely vegetated sites at all source/receiver separation distances are shown in Figs. 6(a)–6(e). As before, the data from Transect 2 are shown for the densely vegetated site. At each range, the spectra for all three replicates of the CSS signals are shown. The black line in the plots is the mean noise level, taken from average spectra calculated from the recording periods directly following the CSS signal. The noise level decreases as a function of receiver range as the hydrophone sensitivity and gain were adjusted (see Table II). The hydrophone recording system noise floor dominates the noise spectra and includes several spectral peaks associated with self-noise of the signal conditioning and recording electronics. The measured signal is below the noise floor for the highest frequencies at the 200 and 400 m source positions.

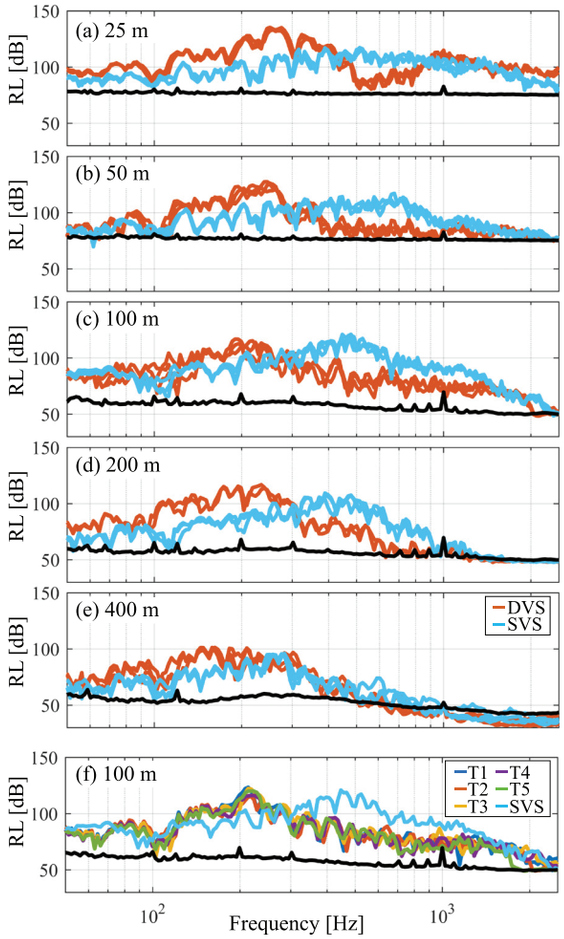

FIG. 6. (Color online) Frequency spectra for the three replicate signals recorded at ranges of (a) 25 m, (b) 50 m, (c) 100 m, (d) 200 m, and (e) 400 m at the densely vegetated site (Transect 2) and at the sparsely vegetated site. (e) Frequency spectra for a single CSS reception at from all five transects at the 100 m range at the densely vegetated site and at the sparsely vegetated site. In all plots, the black curve is the average noise level.

https://doi.org/10.1121/10.0000954

An examination of the spectra reveals the similarity of the replicates, which is an indication of the repeatability of the CSS signal as well as stationary conditions over the measurement interval. Comparing the measurements between the two sites, the data recorded at the densely vegetated site have comparably more low-frequency content. For the closest source positions, the signals recorded in the densely vegetated have spectral peaks around 250 Hz, whereas the signals recorded in the sparsely vegetated site have spectral peaks around 450 Hz. For both sites, the higher frequency content of the signals is attenuated at the more distant CSS positions.

The spectra of all five transects at the densely vegetated site and the single transect at the sparsely vegetated site at a range of 100 m are shown in Fig. 6(f). There is very little variability among all the measurements recorded at the densely vegetated site. These data appear to oppose the observations of other researchers who documented the diurnal dependence of the acoustic response as described in Sec. I C. However, as shown by the broadband measurements reported in Lee *et al.* (2019), frequencies below 3 kHz were nearly unaffected by the time of day. Note, the data reported in Lee *et al.* (2019) were recorded simultaneously at the same sites as the data presented in the current paper.

III. RESULTS

A. Analytical estimate of void fraction

Although the focus of this work is the application of Bayesian inference techniques to characterize the relative productivity of the seagrass meadow, this section explores an approximate method to analytically calculate the void fraction of gas present. The environment is modeled as a Pekeris waveguide, which includes a fluid layer modeled with an effective sound speed representative of a bubbly liquid over a fluid half space representing the bottom. The first step is to calculate the effective sound speed in the fluid layer from an estimate of the modal cutoff frequency, which is the lower frequency limit corresponding to guided waves whose energy is concentrated in the water layer by total reflection, and whose amplitude in the underlying half space falls off exponentially with distance from the interface. The second step is to calculate the void fraction of gas in the water layer using Eq. (11), the Mallock-Wood equation.

For a Pekeris waveguide, the modal cut-off frequency f_c of mode 1 is calculated according to (Choi and Dahl, 2006)

$$f_c = \frac{c_w}{4d}\frac{1}{\sqrt{1-(c_w/c_b)^2}}, \tag{12}$$

where c_w is the sound speed in the water layer, c_b is the sound speed in the bottom, and d is the waveguide depth. This equation was solved for sound speed in the water layer c_w, using sound speed in the bottom c_b determined from the arrival time of the CSS signals (see Fig. 5), the measured water depth (see Table III), and the estimated the modal cutoff frequency f_c from the spectra of the CSS signals (see Fig. 6).

TABLE III. Parameters to estimate void fraction using the analytical approach.

Site and transect number	Modal cutoff frequency (Hz)	Water depth (m)	Sound speed (m/s)	Void fraction
DVS Transect 1	251	1.40	947	9.6216×10^{-5}
DVS Transect 2	268	1.35	979	8.6306×10^{-5}
DVS Transect 3	283	1.25	977	8.7297×10^{-5}
DVS Transect 4	251	1.15	909	1.1009×10^{-4}
DVS Transect 5	253	1.10	886	1.1801×10^{-4}
SVS Transect 1	564	0.85	1201	3.7748×10^{-5}

For the short ranges considered in this work, it was not possible to separate modal arrivals using a short-time Fourier transform approach. Hence, the modal cut-off frequency f_c of mode 1 was estimated from the measured spectra of the signals from the closest two CSS positions (25 and 50 m). The cut-off frequency was estimated as 10 Hz below the spectral peak since the Airy phase portion of the arrival typically has low signal-to-noise ratio (SNR). The 10 Hz offset from the spectral peak is consistent with published results (Wan *et al.*, 2018) as well as with simulations of the simplified propagation environment studied here.

The median frequency from the six spectra (three replicates × two CSS positions) was used as the estimate for f_c. The spectral peak is formed near modal cut-off frequency f_c of mode 1, because there are no propagating modes at lower frequencies. Below the modal cutoff frequency of the first mode, a modal continuum exists. However, the energy in these continuum modes is rapidly attenuated into the bottom, and they do not contribute to the field except at very short ranges. For the modes that propagate in the water layer at frequencies above the mode 1 cutoff frequency, the effects of scattering and absorption due to bubbles increase with frequency. Together, these effects produce a spectral peak near the cutoff frequency for mode 1.

The estimated effective water column sound speeds calculated from the cut-off frequency of mode 1 according to Eq. (12) are listed in Table III. The estimated speeds at the densely vegetated site show a trend of decreasing sound speed throughout the day, with the range of estimated speeds being about 100 m/s. The estimated effective speed at the sparsely vegetated site is more than 200 m/s greater than the mean of the estimated effective speeds at the densely vegetated site, and closer to the directly measured water sound speed.

The next step is to use the Mallock-Wood equation, Eq. (11), to estimate the void fraction of gas β present in the waveguide. In applying Eq. (11) to estimate the value of β, bulk moduli of air and seawater were calculated according to $B_g = \gamma p_A$ and $B_w = \rho_w c_w^2$, where the value of $c_w = 1542$ m/s was calculated from measurements of temperature and salinity, and tabulated values were used for the density of seawater $\rho_w = 1029\,\text{kg/m}^3$ and density of air $\rho_g = 1.225\ \text{kg/m}^3$, and the ratio of specific heats $\gamma = 1.4$. Hydrostatic pressure p_A

corresponding to 1-m water depth of the seagrass canopy was used.

Using the effective sound speeds estimated from the spectra of the CSS signals, the estimated void fractions are given in Table III. On average, the estimated void fractions at the seagrass site increase throughout the day, showing a 30% change between the minimum void fraction estimated in the morning and the maximum void fraction measured in the late afternoon. The void fraction estimated at the sparsely vegetated site is less than half of the void fraction measured at the densely vegetated site at approximately the same time of day.

B. Bayesian inference of the void fraction

This work utilizes a Bayesian inference method to estimate the posterior probability distributions (PPDs) of environmental parameters, most notably the void fraction of gas present in the water column. In a Bayesian formulation, the complete solution to an inference problem is characterized by the PPD of the unknown model parameters. This section summarizes the Bayesian formulation of inference theory and the approach used for numerical integration of the PPD. Overviews of Bayesian inference applied to geophysical inference problems are given by Tarantola (2005) and Sen and Stoffa (1995).

1. Inference theory

Let $\mathbf{m}$ and $\mathbf{d}$ represent model and data vectors, respectively, with elements m_i and d_i considered to be random variables. "Bayes" rule may be expressed as

$$\mathcal{P}(\mathbf{m}|\mathbf{d}) \propto \mathcal{P}(\mathbf{d}|\mathbf{m})\mathcal{P}(\mathbf{m}), \tag{13}$$

where the conditional probability $\mathcal{P}(\mathbf{m}|\mathbf{d})$ represents the PPD of the unknown model parameters given the observed data $\mathcal{P}(\mathbf{d}|\mathbf{m})$ and prior information $\mathcal{P}(\mathbf{m})$. Interpreting the conditional probability $\mathcal{P}(\mathbf{d}|\mathbf{m})$ for the measured data defines the likelihood function $\mathcal{L}(\mathbf{m})$, which, for the common assumption of unbiased Gaussian errors, can be expressed as $\mathcal{L}(\mathbf{m}) \propto \exp[-\mathcal{E}(\mathbf{m})]$, where $\mathcal{E}(\mathbf{m})$ is the error function. Hence, the PPD can be expressed as

$$\mathcal{P}(\mathbf{m}|\mathbf{d}) \propto \frac{\exp[-\mathcal{E}](\mathbf{m})\mathcal{P}(\mathbf{m})}{\int \exp[-\mathcal{E}](\mathbf{m}')\mathcal{P}(\mathbf{m}')d\mathbf{m}'}, \tag{14}$$

where the domain of integration spans the model parameter space.

The multidimensional PPD is interpreted in terms of properties defining parameter estimates and uncertainties, such as the *maximum a posteriori* (MAP) $\hat{\mathbf{m}}$ estimate and marginal probability distributions, defined as

$$\hat{\mathbf{m}} = \mathrm{Arg}_{\max}[\mathcal{P}(\mathbf{m}|\mathbf{d})], \tag{15}$$

$$\mathcal{P}(m_i|\mathbf{d}) = \int \delta(m_i' - m_i)\mathcal{P}(\mathbf{m}'|\mathbf{d})d\mathbf{m}', \tag{16}$$

where δ is the Dirac delta function.

To evaluate the multi-dimensional integrals of the PPD in an efficient manner, importance sampling is applied (Dosso and Nielsen, 2002a). The goal of importance sampling is to choose a simple, unbiased, practical function that satisfies the normalization condition [the denominator of Eq. (15)] and avoids an exhaustive search of the model space. The fast Gibbs sampler (FGS) achieves this goal by employing the Metropolis algorithm to generate $\mathcal{P}(m_i|\mathbf{d})$ as the importance sampling function. Thus, unbiased estimates of the marginal probability distributions are computed directly from the set of Q models, with no requirement to weight the samples by estimated probabilities

$$\mathcal{P}(m_i|\mathbf{d}) \approx \frac{1}{Q}\sum_{i=1}^{Q} \delta(m_i' - m_i)\mathcal{P}(\mathbf{m}'|\mathbf{d})d\mathbf{m}'. \tag{17}$$

Following a previous application of the FGS algorithm, as detailed in Ballard *et al.* (2018a), convergence is accelerated using simulated annealing (SA) methods.

2. Environmental parametrization

The environment was parametrized as an isovelocity water column over a bottom consisting of a single isovelocity layer over a half space. A horizontally stratified environment was assumed. Geometric parameters including source depth, receiver depth, and water depth, were measured during the experiment and were fixed to the measured values when computing the PPDs for the geoacoustic parameters. However, due to uncertainty in the source waveform measurement from interference from bottom and surface reflections on the source monitor hydrophone recordings, the source level was included as an unknown parameter in the inference.

A frequency-dependent sound speed and attenuation in the water layer were inferred using the frequency-dependent effective medium model for bubbly liquids (Commander and Prosperetti, 1989) given in Sec. I B. Because the depth of the water column (from 0.8 to 1.4 m) was appreciably smaller than the wavelength of the peak frequency of the received signals ($\lambda_{\mathrm{peak}} = 6$ m for the densely vegetated site and $\lambda_{\mathrm{peak}} = 3$ m for the sparsely vegetated site), the water column was modeled as isovelocity. Although the seagrass canopy is physically limited to the lower 30 cm of the water column, free bubbles were routinely observed in the water layer above the canopy. Hence, the environment was parametrized as a single layer characterized by a void fraction with Gaussian distributed bubble radii. In the sediment layer and half space, a frequency-independent sound speed was assumed and attenuation was modeled with a linear dependence on frequency. These are the usual assumptions for marine sediments (Chapman *et al.*, 2003; Dettmer *et al.*, 2010; Dosso and Nielsen, 2002b; Hermand, 1999; Holland and Osler, 2000).

Uniform prior distributions were assumed for all parameters, and the search bounds are listed in Table IV. The densities in the sediment layer and lower half space were set to 1.6 and 1.8 g/cm^3, respectively. These values are typical of fine- and coarse-grained sandy sediments. Initial inversions found

https://doi.org/10.1121/10.0000954

TABLE IV. Parameter search bounds and inference results. MAP estimates and 68% confidence intervals are listed for each of the five transects at the densely vegetated site (first five values listed) and for the single data collection at the sparsely vegetated site.

Parameter	Search bounds	MAP estimate	68% Confidence interval
source level (dB)	[220 240]	230 / 229 / 231 / 230 / 227 / 221	[226 234] / [225 233] / [225 233] / [227 235] / [224 232] / [220 225]
mean bubble radius (μm)	[50 1000]	112 / 160 / 112 / 112 / 160 / 304	[64 544] / [64 544] / [64 544] / [64 496] / [64 448] / [112 640]
standard deviation of the bubble radius (μm)	[20 500]	56 / 128 / 176 / 80 / 80 / 128	[32 320] / [32 320] / [32 296] / [32 320] / [32 272] / [32 320]
void fraction (1×10^{-4})	[0 1]	0.932 / 0.977 / 0.927 / 1.00 / 1.04 / 0.233	[0.852 1.02] / [0.813 0.977] / [0.841 1.02] / [0.922 1.09] / [0.886 1.13] / [0.192 0.419]
sediment layer thickness (m)	[2 40]	27.7 / 29.6 / 29.6 / 22.0 / 27.7 / 22.0	[14.4 31.5] / [18.2 35.3] / [18.2 37.2] / [12.5 29.6] / [22.0 37.2] / [8.7 29.6]
sediment layer sound speed (m/s)	[1500 2000]	1763 / 1788 / 1763 / 1713 / 1763 / 1663	[1638 1863] / [1663 1888] / [1638 1863] / [1638 1863] / [1663 1913] / [1563 1788]
sediment layer attenuation (dB/λ)	[0.00 0.40]	0.35 / 0.31 / 0.29 / 0.29 / 0.27 / 0.21	[0.25 0.37] / [0.23 0.35] / [0.23 0.37] / [0.19 0.33] / [0.19 0.35] / [0.17 0.31]
sediment half space sound speed (m/s)	[2000 2800]	2165 / 2698 / 2575 / 2452 / 2657 / 2288	[2083 2575] / [2288 2739] / [2247 2739] / [2124 2616] / [2247 2739] / [2083 2575]

that the data were insensitive to the attenuation in the sediment half space, and it was fixed with a value of 0.10 dB/λ.

3. Propagation modeling

A normal-mode model (Westwood *et al.*, 1996) was used to calculate the acoustic field for frequencies up to 2.5 kHz. The nonlinear frequency dependence of sound speed and attenuation in the water layer was included in the propagation model by calculating the modal eigenvalues and eigenfunctions over frequency intervals for which the value of sound speed was held constant, and linear frequency dependence was assumed for attenuation. The bounds of the intervals were designated by descretizing the attenuation profile into 1/4 dB/λ steps, since over the frequency band considered, the variability in attenuation dominated that of the sound speed. The calculated time series were obtained from the inverse Fourier transform of the frequency domain solutions multiplied by the CSS spectrum.

4. Error function

An error function quantifies the difference between the measured and modeled data. In this analysis, the error function was heuristically constructed to have sensitivity to both the structure and the energy level of the measured time series. The formulation of the error function follows that of previous work (Sagers and Knobles, 2014). A normalized cross-correlation with a restricted time lag of 7 ms was used to evaluate the similarity of the arrival structure; this cost function was sensitive to the arrival time and frequency content of the measured signal. The normalized cross-correlation error function is given by

$$\mathcal{E}_{\mathrm{c}} = \langle 1 - p_i^{\mathrm{meas}} \star p_i^{\mathrm{mod}} \rangle_i, \tag{18}$$

where p_i^{meas} and p_i^{mod} are the measured and modeled time series, the symbol $\star$ signifies the normalized cross correlation at time τ_{p}, and $\langle\rangle_i$ is an average over the events.

A difference of the spectral levels was used to compare the received energy level. This part of the cost function was necessary because the effective attenuation due to bubbles had the effect of modifying the received level of the calculated time series by several orders of magnitude. The spectral difference was calculated for decidecadal bands between 100 Hz and 2.5 kHz, excluding bands with negative SNR which occurred at higher frequencies for the more distant CSS positions. The spectral difference error function is given by

$$\mathcal{E}_{\mathrm{d}} = \left\langle \sum (s_i^{\mathrm{meas}} - s_i^{\mathrm{mod}}) \right\rangle_i, \tag{19}$$

where s_i^{meas} and s_i^{mod} are the spectral levels in decidecadal bands of the measured and modeled time series. The total error function was given as a geometric mean of the normalized cross-correlation error function and the spectral difference error function,

$$\mathcal{E} = \sqrt{\mathcal{E}_{\mathrm{c}} \mathcal{E}_{\mathrm{d}}}. \tag{20}$$

5. Marginal probability distributions

The marginal probability distributions are shown in Fig. 7 and the *maximum a posteriori* (MAP) estimates and 68% confidence intervals are listed in Table IV. The narrowest distributions were found for the void fraction in the water layer. The MAP estimates of the void fraction for the five data sets recorded at the densely vegetated site ranged from 9.27×10^{-5} to 1.04×10^{-4}, whereas the MAP estimate at the sparsely vegetated site was 2.33×10^{-5}, less than a quarter of the void fraction estimated at the densely vegetated site at the same time of day.

In addition to having a substantially lower MAP estimate, the marginal probability distribution for the void fraction at the sparsely vegetated site also shows much greater uncertainty than the values at the densely vegetated site. While the lower void fraction is attributed to the overall lower coverage of seagrass, the increased uncertainty is believed to be caused by range-dependence of seagrass coverage along the propagation path. As shown by the satellite imagery in Fig. 2(c), significant variability can be observed especially near the 400 m CSS location where the seagrass coverage appears much more dense. Additionally, the assumption of range-independence is also challenged by the higher received level recorded at a range of 100 m [see Fig. 5(b)].

The marginal probability distributions for the bubble size parameters show a slight trend towards small bubbles with a narrow size distribution; however, overall, the marginals for the bubble size parameters are uninformative. The low-frequency data considered in the inversion are below the individual bubble resonance frequency. Within this frequency band, the effective sound speed is primarily influenced by the void fraction, and it is less affected by the sizes of the bubbles.

The acoustic data also show some sensitivity to the source level and the sound speed and attenuation in the sediment layer. For the estimates from the densely vegetated site, the MAP estimates are consistently near a level of 230 dB, which is slightly greater than the expected source level for a CSS chamber of this size and deployed at 0.5 m depths. An examination of the joint marginal probability distributions showed correlations between source level and sound attenuation in the sediment layer, indicating that a higher source level may be compensating for an overestimate in that sediment attenuation. The source level estimated at the sparsely vegetated site was better aligned with expectations and was also associated with a lower attenuation in the sediment layer.

The sound speed in the sediment layer was consistently estimated around 1760 m/s for all five transects at the densely vegetated site, and the estimated value was 100 m/s lower at the sparsely vegetated site. These estimates are consistent with the sound speeds estimated from travel time in Sec. II C. Sediment sound speed in the lower half space was not well-resolved by the inference, although the results for all transects and environments favor a sound speed greater than 2100 m/s. The results for the thickness of the sediment layer also display a high degree of uncertainty, although it is clear that a relatively thick (>20 m) layer is preferred.

Estimates for the frequency dependence of sound speed and attenuation in the water layer along with their associated uncertainties are displayed in Fig. 8. These results were calculated from the set of Q accepted models according to Eq. (17), but replacing the model parameter m_i with sound speeds and attenuation calculated from Eqs. (9) and (10). Thus, the data in Fig. 8 represent a set of derived marginal probability distributions, since the distributions are based on quantities calculated from the model parameters instead of the parameters themselves. Since the PPDs were computed

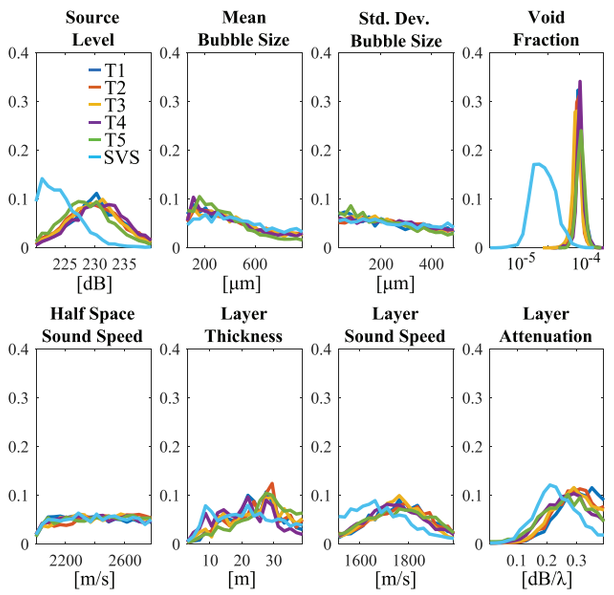

FIG. 7. (Color online) Marginal probability distributions of the inferred parameters determined for measurements at the densely vegetated sites (listed as Transects 1–5 in the legend) and at the sparsely vegetated site (listed as SVS in the legend).

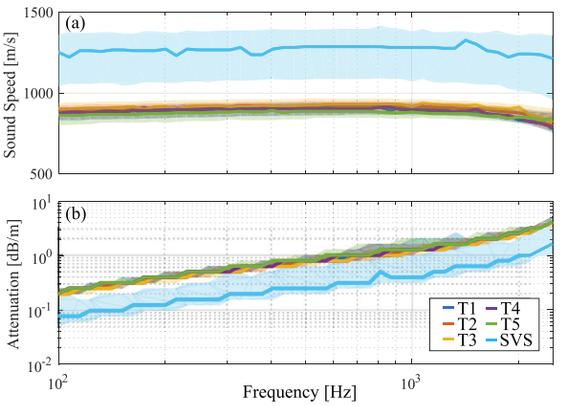

FIG. 8. (Color online) Frequency-dependent sound speed and attenuation in the water layer calculated using the effective medium model for bubbly liquids determined from measurements at the densely vegetated sites (listed as Transects 1–5 in the legend) and at the sparsely vegetated site (listed as SVS in the legend). The solid lines represent the derived MAP estimates and the shaded areas represent 68% confidence intervals.

https://doi.org/10.1121/10.0000954

TABLE V. Derived MAP estimates and 68% confidence intervals for sound speed and attenuation at a frequency of 1 kHz.

Site and transect number	Sound speed (m/s)		Attenuation (dB/m)	
	MAP est.	68% Confid. interval	MAP est.	68% Confid. interval
DVS Transect 1	893	[868 938]	1.260	[1.048 1.662]
DVS Transect 2	913	[888 948]	1.097	[1.000 1.447]
DVS Transect 3	918	[888 963]	1.097	[0.955 1.447]
DVS Transect 4	897	[863 938]	1.149	[1.048 1.662]
DVS Transect 5	883	[843 928]	1.319	[1.149 1.822]
SVS Transect 1	1283	[1073 1383]	0.549	[0.316 1.048]

from a distribution of dispersion curves, each having a unique frequency dependence, the resulting MAP estimates and uncertainty envelopes display a non-smooth frequency dependence that is not characteristic of an individual dispersion curve.

As shown in Fig. 8(a), for results from all six inferences (five transects at the densely vegetated site and the single data collection at the sparsely vegetated site), the sound speed shows little variation with frequency. As predicted from the close agreement in estimates of the void fraction at the densely vegetated site, there is also close agreement in the sound speeds estimated at the densely vegetated site. This contrasts with the sound speed estimated at the sparsely vegetated site, which is significantly higher and closer to the speed of the bubble-free water. The sound speed at the sparsely vegetated site is also characterized by a larger confidence interval, which is directly related to the uncertainty in the estimated void fraction. For reference, the MAP estimates and 68% confidence intervals for sound speed at a frequency of 1 kHz are listed in Table V.

The frequency-dependent attenuation is shown in Fig. 8(b). Within this frequency band, attenuation increases monotonically with frequency with an exponential frequency dependence of 0.72 for the densely vegetated site measurements and 0.88 for the sparsely vegetated site measurement. As before, the greater uncertainty in the attenuation at the sparsely vegetated site is attributed to greater uncertainty in the void fraction at that site.

IV. DISCUSSION

A. Comparison of analytically calculated and inferred void fractions

Figure 9 compares the void fractions estimated using the analytic approach described in Sec. III A and the Bayesian approach described in Sec. III B. First, note similarities in the estimates obtained from the two approaches. Both techniques produce significantly higher estimates of the void fraction at the densely vegetated site compared to that of the sparsely vegetated site. Additionally, both approaches produce their highest estimates of the void fraction for the two measurements made during the latter portion of the day at the densely vegetated site.

However, differences can also be observed in the estimates obtained from the two different techniques. For the estimates corresponding to the densely vegetated site, the estimated void fraction determined by the analytical approach is biased low compared to estimates obtained with the Bayesian approach. One reason for this is the simplified environment used by the analytical approach, which included only a water layer over an acoustic half space. For the case of the densely vegetated site, including a sediment layer over a faster subbottom half space produces a lower modal cut-off frequency. The decreased modal cut-off frequency results in a lower estimate for the effective water column sound speed, which is associated with a higher void fraction. The increase in the estimated void fraction brings the analytical result into better agreement with the estimate obtained with the Bayesian approach.

For the case of the sparsely vegetated site, the spectral peak did not provide a good estimate for the modal cut-off frequency of mode 1. The comparatively lower loss in the water column did not sufficiently attenuate the higher order modes as it did for the densely vegetated site. Hence, the error in the analytical method is attributed to a poor estimate of the cut-off frequency.

Despite its shortcomings, the analytical approach for estimating the void fraction was extremely computationally efficient. Furthermore, the results from the Bayesian inversion supported the assumption of an approximately frequency-independent sound speed within the low-

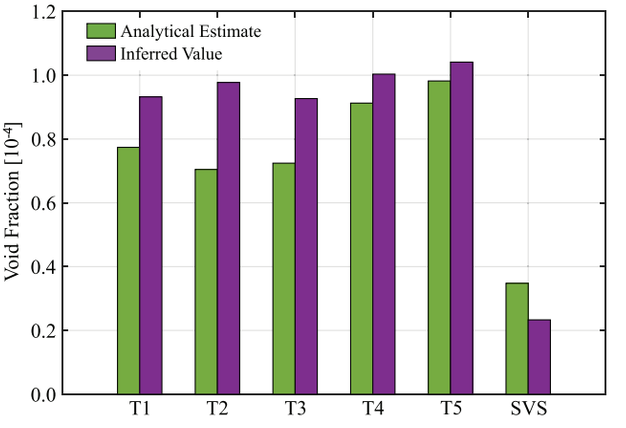

FIG. 9. (Color online) Comparison of the void fraction estimated using the analytic approach described in Sec. III A and the Bayesian approach described in Sec. III B. Results are shown for the densely vegetated sites (labeled as Transects 1–5) and at the sparsely vegetated site (labeled as SVS).

frequency measurement band [see Fig. 8(a)]. Provided with foreknowledge of the bottom properties (including subbottom layering), these parameters could be accounted for in relating the modal cut-off frequency to the water column sound speed. This could be the case in a monitoring application for which the environment was intensely characterized at the beginning of the study, and the analytic approach was applied to quantify changes in the environment over time.

Although much more computationally intensive, the Bayesian approach has several advantages. In this work, it facilitated a more complex model for the seagrass the included the frequency dependence of sound speed and attenuation of the bubbles in the water layer. The cost functions were designed to be sensitive to both the arrival time and structure of the acoustic time series as well as the attenuating effects of seagrass bubbles in the frequency domain. The Bayesian approach also provided a measure of the uncertainty of the estimated model parameters through the marginal probability distributions. Furthermore, the joint probability distributions were examined to understand correlations between the estimated parameters.

B. Comparison to measured environmental parameters

By design, the densely and sparsely vegetated sites were chosen to have similar environmental conditions so as to isolate the effects of seagrass on the acoustic measurements. Solar irradiance measured at the two sites [see Fig. 3(a)] was almost identical, except for a few clouds that passed over the densely vegetated site. The level of dissolved oxygen was slightly higher at the densely vegetated site [see Fig. 3(b)], but this parameter is directly related to the presence of seagrass. Likewise, the slightly warmer water temperatures at the sparsely vegetated site [see Fig. 3(c)] may be attributed to the lack of a seagrass canopy which mitigates water temperatures through the insulating effect of gas volumes encapsulated in the seagrass tissue. Nevertheless, the small change in sound speed due to the differences in water temperature is small compared to the large changes in the effective sound speed due to the presence of gas volumes in the water layer.

The water depth was shallower at the sparsely vegetated site [see Fig. 3(d)]. However, the 30 cm change in water depth over the course of the day at the densely vegetated site exceeded the difference between the minimum depth at the densely vegetated site and that of the sparsely vegetated site, which was 25 cm. Finally, the wind speed and direction [see Figs. 3(e) and 3(f)] were comparable at both measurement sites, and no breaking waves were observed at either location.

Hence, the large differences in the estimated void fractions observed between the two sites are attributed to the acoustical effects of the seagrass meadow. Furthermore, contrary to broadband (Lee *et al.*, 2019) and higher frequency measurements (Chang *et al.*, 2019; Felisberto *et al.*, 2015; Hermand, 2004; Hermand *et al.*, 1998), which documented a large change in the received level of acoustic signals associated with diurnal effects of oxygen production, this analysis produced almost constant estimates of void fraction from the data collected over the course of a day at the densely vegetated site. Therefore, the observed acoustical effects are attributed to the gas volumes trapped within the seagrass leaves, roots, and rhizomes.

Although minimal, within the low-frequency data analyzed in this study, some small diurnal effects are observed. For Transects 4 and 5 at the densely vegetated site, which were collected after the dissolved oxygen level had surpassed 100%, a slight increase in the estimated void fraction was found by both the analytical and Bayesian methods (see Fig. 9). This increase in the void fraction is attributed to the photosynthetic processes which produce oxygen as a byproduct and emit free bubbles into the water column.

C. Implications of the simplified model

The inference of geoacoustic parameters requires the assumption of a forward model describing the observed physical system. When the physical model is a poor approximation of the actual environment, the resulting parameter estimates and uncertainties may be biased. This work utilized a mathematical model for the propagation of acoustic waves in water containing Gaussian-distributed, free, spherical bubbles (Commander and Prosperetti, 1989) to calculate the frequency-dependent sound speed and attenuation. However, as described in Sec. I A, seagrass possess a complicated system of lacunae that transfers gas throughout the plant. Considering that low-frequency acoustical effects observed in this work are most likely associated with gas encapsulated within its leaves, roots, and rhizomes, the use of a model for sound propagation through a liquid containing free, spherical bubbles may not be appropriate. The same conclusion was drawn from laboratory measurements which demonstrated the importance of seagrass tissue elasticity and structure on the acoustic properties of seagrass leaves (Wilson *et al.*, 2010). The results from this study indicated that a model that accounts for aspherical gas bodies constrained within the plant tissue is needed to produce more accurate results. A model for encapsulated bubbles exists (Church, 1995), but the elastic properties of the plant tissue have not been adequately quantified to justify the use of such a model. It is also possible to account for nonspherical bubble shapes (Spratt *et al.*, 2017), but a complete statistical quantification of the bubble shape parameters has not been completed. New mathematical models that account for the encapsulation of gas channels by the seagrass tissue, as well as the shapes of lacunae, are needed to accurately predict acoustic propagation through seagrass.

Nevertheless, some observations can be made about the effects of including an elastic shell and accounting for the elongated bubble shape. First, for a given set of bubble size parameters, the addition of an elastic shell which possesses finite rigidity will cause the bubble resonance frequency to increase. Hence, within the construct of the encapsulated bubble model (Church, 1995), there exists an effective

https://doi.org/10.1121/10.0000954

sound speed that is lower than the sound speed of the bubble-free water and constant over the low-frequency band considered in this work. Likewise, as demonstrated for the case of a prolate spheroid bubble, the resonance frequency is increased as the aspect ratio (length-to-width ratio) of the bubble is increased (Spratt *et al.*, 2017). Additionally, for frequencies well below the individual bubble resonance frequency, for a given void fraction, the addition of an elastic shell alters the damping effects of the bubbles, so that a higher void fraction is needed to obtain equivalent sound speed and attenuation values (Church, 1995). Therefore, the estimated void fractions obtained in this work are likely biased low. This hypothesis is consistent with laboratory measurements that used effective medium models to estimate the void fraction of *T. testudinum* leaves and rhizomes. The acoustically estimated void fractions were compared to microscopy measurements of the gas cavities, and the acoustically determined values were 6.8 times lower for the leaves and 28 times lower for the stiffer rhizomes (Wilson and Dunton, 2009). Despite these shortcomings, its promising that more complex models could be applied within the Bayesian framework to achieve more accurate results.

D. Other sources of entrained gas

Another assumption applied in the geoacoustic inference was that the seagrass was the only source of gas bubbles in the environment. However, it is well known that seagrass meadows are home to many animals, including fish, which may contain swim bladders. The acoustical effects of swim bladders, including scattering and extinction cross-sections, damping factors, and resonance frequencies, have been the focus of many bubble-related studies (see Ainslie and Leighton, 2011, and references therein). Furthermore, Diachok (1999) demonstrated absorption losses at the resonance frequencies of sardines' gas bladders could be observed in propagation measurements. Therefore, neglecting acoustical effects of fish with swim bladders will bias the estimated void fraction of gas attributed seagrass.

However, it is unlikely that the presence of fish is dominating the estimates presented in this paper. Although numerous fish were observed at the densely vegetated site, their collective gas volume does not rival that of the seagrass meadow. By examining underwater photographs of the seagrass meadow taken during the experiment, an upper bound of twenty 12-cm-long fish per cubic meter was estimated. With each fish having a swim bladder with an effective radius of 5 mm, the void fraction of gas resulting from swim bladders would be approximately 10^{-5}. This estimate is an order of magnitude less than the estimated void fraction of gas in the seagrass at the densely vegetated site (see Table IV). Additionally, a comparison of the estimated attenuation through the seagrass meadow, which was on the order of 1 dB/m at 1 kHz, is more than two orders of magnitude greater than the attenuating effects of schools of sardines in the same frequency band (Diachok, 1999).

V. CONCLUSIONS

Acoustic remote sensing techniques were applied to characterize two different regions of a seagrass meadow: a densely vegetated meadow of *T. testudinum* and a sandy region sparsely populated by isolated stands of *T. testudinum*. A computationally efficient analytic approach provided an approximate estimate of the void fraction of gas present in the seagrass-containing water layer. The application of the technique was complicated by challenges in estimating the modal cut-off frequency from the short-range propagation data, and limited by the assumption of a simple Pekeris waveguide. Nevertheless, the estimated void fractions were consistent with expected trends such as a higher void fraction at the densely vegetated site and a slight increase in the estimated gas volume in during the periods of highest irradiance when the dissolved oxygen in the water surpassed 100%.

A Bayesian approach provided a more comprehensive solution to the inference problem. The nonlinear approach allows for a more complicated representation of the environment, which in this case included modeling the water layer as a bubbly liquid with a frequency-dependent sound speed and attention and a sediment layer over a semi-infinite acoustic half space. In the Bayesian formulation, the complete solution is characterized by the PPD of the unknown model parameters and the marginal probability distributions were examined to indicate the resolution of the estimated void fractions. A comparison of the void fractions estimated at the densely vegetated and sparsely vegetated sites showed that the estimated void fractions were well-resolved. Within the densely vegetated site, the distributions were overlapping, and although the MAP estimates indicated a slight increase in the estimated void fraction during the periods of highest irradiance, the diurnal changes are within the uncertainty of the estimates.

The void fractions estimated using the Bayesian approach range from 2.33×10^{-5} at the sparsely vegetated site to 1.04×10^{-4} in the late afternoon at the densely vegetated site. Comparing the result from the densely vegetated site that of previous work (Ballard *et al.*, 2018b), shows a decrease in the estimated void fraction by a factor of two. As described in Sec. I C, the earlier data set was collected one year prior in the month of July. While range-dependence of seagrass productivity within the meadow may be a factor, these results may also point to seasonal variability as the higher void fraction was estimated during the annual peak of seagrass productivity (Kaldy and Dunton, 2000).

The void fractions estimated in this study are within the range of values hypothesized by Hermand in his original work (Hermand *et al.*, 2000). Furthermore, modeling-based approaches, such as those advocated by Hermand and the methods put forth in this work, can account for all characteristics of the waveguide that affect the acoustic propagation. Hence, within the limits of the assumptions, the estimated parameter values are absolute, as opposed to empirically-based estimates which must be tuned to each new environment (Felisberto *et al.*, 2015).

These results demonstrate the potential use of acoustical methods to remotely sense seagrass productivity. The sensitivity of sound to the void fraction of gas present in the seagrass meadow was established as illustrated by the narrow marginal probability distributions that provided distinct estimates of the void fraction between the densely and sparsely vegetated sites. Acoustical techniques could be used to survey large areas to characterize the relative density of seagrass in different parts of the same meadow, or to compare between meadows. Alternatively, an acoustic measurement system could be set up to monitor a single location to access changes in the meadow over time, including the meadow's response to diurnal and season changes, as well as discrete forcing events such as storms or a pollution spill.

Future work will address inaccuracies in the forward modeling assumptions, specifically the use of a free-bubble model to represent the gas encapsulated within the elongated channels of the seagrass tissue. This task requires new mathematical models that account for the shapes of lacunae, and new measurements of the elastic moduli and other material parameters of the seagrass tissue. Additionally, plans to extend the application of these methods to higher frequencies will make it possible to sense diurnal effects of photosynthetic activity. These increased modeling capabilities will make it possible to differentiate between bubbles encapsulated within the seagrass tissue, which are continuously present, and bubbles free-floating in the water, which are typically present during periods of high irradiance and related to increased photosynthetic activity.

ACKNOWLEDGMENTS

This work was supported by the ARL:UT Independent Research and Development Program and by the Office of Naval Research (ONR) Ocean Acoustics Program under Grant No. N00014-18-1-2401.

Ainslie, M. A., and Leighton, T. G. (**2011**). "Review of scattering and extinction cross-sections, damping factors, and resonance frequencies of a spherical gas bubble," J. Acoust. Soc. Am. **130**(5), 3184–3208.

Allaoui, N. E., Serra, T., Colomer, J., Soler, M., Casamitjana, X., and Oldham, C. (**2016**). "Interactions between fragmented seagrass canopies and the local hydrodynamics," PLoS One **11**, 1–19.

Ballard, M. S., Costley, R. D., Sagers, J. D., Lee, K. M., McNeese, A. R., Hathaway, K. K., Wilson, P. S., and Smith, E. W. (**2018a**). "A comparison between directly measured and inferred wave speeds from an acoustic propagation experiment in Currituck Sound," J. Acoust. Soc. Am. **143**, 237–247.

Ballard, M. S., Lee, K. M., Sagers, J. D., Venegas, G. R., McNeese, A. R., Rahman, A. F., Dubin, J. T., and Wilson, P. S. (**2018b**). "Measurements and modeling of acoustic propagation in a seagrass meadow," Proc. Mtg. Acoust. **33**(1), 005002.

Chang, A. Y. Y., Chiu, L. Y. S., Mok, M. H. K., Soong, K., and Huang, W. J. (**2019**). "Experimental observations of diurnal acoustic propagation effects in seagrass meadows on the Dongsha Atoll," J. Acoust. Soc. Am. **146**(3), EL279–EL285.

Chapman, N. R., Chin-Bing, S., King, D., and Evans, R. B. (**2003**). "Benchmarking geoacoustic inversion methods for range dependent waveguides," IEEE J. Oceanic Eng. **28**(3), 320–330.

Choi, J. W., and Dahl, P. H. (**2006**). "First-order and zeroth-order head waves, their sequence, and implications for geoacoustic inversion," J. Acoust. Soc. Am. **119**(6), 3660–3668.

Church, C. C. (**1995**). "The effects of an elastic solid surface layer on the radial pulsations of gas bubbles," J. Acoust. Soc. Am. **97**(3), 1510–1521.

Commander, K. W., and Prosperetti, A. (**1989**). "Linear pressure waves in bubbly liquids: Comparison between theory and experiments," J. Acoust. Soc. Am **85**(2), 732–746.

Dettmer, J., Dosso, S. E., and Holland, C. W. (**2010**). "Trans-dimensional geoacoustic inversion," J. Acoust. Soc. Am. **128**(6), 3393–3405.

Diachok, O. (**1999**). "Effects of absorptivity due to fish on transmission loss in shallow water," J. Acoust. Soc. Am. **105**(4), 2107–2128.

Dosso, S. E., and Nielsen, P. L. (**2002a**). "Quantifying uncertainty in geoacoustic inversion. I. A fast Gibbs sampler approach," J. Acoust. Soc. Am. **111**(1), 143–159.

Dosso, S. E., and Nielsen, P. L. (**2002b**). "Quantifying uncertainty in geoacoustic inversion. II. Application to broadband, shallow-water data," J. Acoust. Soc. Am. **111**(1), 129.

Dunton, K. H., and Schonberg, S. V. (**2002**). "Assessment of propeller scarring in seagrass beds of the South Texas Coast," J. Coastal Res. **37**, 100–110.

Felisberto, P., Jesus, S. M., Zabel, F., Santos, R., Silva, J., Gobert, S., Beer, S., Björk, M., Mazzuca, S., Procaccini, G., Runcie, J. W., Champenois, W., and Borges, A. V. (**2015**). "Acoustic monitoring of O2 production of a seagrass meadow," J. Exp. Mar. Biol. Ecol. **464**, 75–87.

Fourqurean, J. W., Duarte, C. M., Kennedy, H., Marbà N, Holmer, M., Mateo, M. A., Apostolaki, E. T., Kendrick, G. A., Krause-Jensen, D., McGlathery, K. J., and Serrano, O. (**2012**). "Seagrass ecosystems as a globally significant carbon stock," Nat. Geosci. **5**, 505–509.

Hermand, J. P. (**1999**). "Broad-band geoacoustic inversion in shallow water from waveguide impulse response measurements on a single hydrophone: Theory and experimental results," IEEE J. Oceanic Eng. **24**(1), 41–66.

Hermand, J. P. (**2004**). "Seagrass photosynthesis observed *in situ* from acoustic measurements," in *Proceedings of the OCEANS 04 Conference*, November 9–12, Kobe, Japan, pp. 433–437.

Hermand, J. P. (**2006**). "Continuous acoustic monitoring of physiological and environmental processes in seagrass prairies with focus on photosynthesis," in *Acoustic Sensing Techniques for the Shallow Water Environment*, edited by A. Caiti, N. R. Chapman, J. P. Hermand, and S. M. Jesus (Springer, New York).

Hermand, J. P., Nascetti, P., and Cinelli, F. (**1998**). "Inversion of acoustic waveguide propagation features to measure oxygen synthesis by posidonia oceanica," in *Proceedings of OCEANS '98*, September 28–October 1, Nice, France, pp. 919–926.

Hermand, J. P., Nascetti, P., and Cinelli, F. (**2000**). "Inverse acoustical determination of photosynthetic oxygen productivity of posidonia seagrass," in *Experimental Acoustic Inversion Methods for Exploration of the Shallow Water Environment* (Springer, Dordrecht, the Netherlands), pp. 125–144.

Holland, C. W., and Osler, J. (**2000**). "High resolution geoacoustic inversion in shallow water: A joint time and frequency domain technique," J. Acoust. Soc. Am. **107**(3), 1263–1279.

Kaldy, J. E., and Dunton, K. H. (**2000**). "Above and below-ground production, biomass and reproductive ecology of Thalassia testudinum (turtle grass) in a subtropical coastal lagoon," Mar. Ecol. Press Ser. **193**, 271–283.

Lee, K. M., Ballard, M. S., Venegas, G. R., Sagers, J. D., McNeese, A. R., Johnson, J. R., Wilson, P. S., and Rahman, A. F. (**2019**). "Broadband sound propagation in a seagrass meadow throughout a diurnal cycle," J. Acoust. Soc. Am. **146**, EL335–EL341.

Long, M. H., Sutherland, K., Wankel, S. D., Burdige, D. J., and Zimmerman, R. C. (**2019**). "Ebullition of oxygen from seagrasses under supersaturated conditions," Limnol. Oceanogr. **65**, 314–324.

Mallock, A. (**1910**). "Damping of sound by frothy liquids," Proc. R. Soc. **84**, 391–395.

McNeese, A. R., Muir, T. G., and Wilson, P. S. (**2012**). "Investigation of a tunable combustive sound source," Proc. Mtg. Acoust. **18**, 070001.

McNeese, A. R., Sagers, J. D., Wilson, P. S., and Knobles, D. P. (**2010**). "An investigation of the combustive sound source," Proc. Mtg. Acoust. **9**, 005002.

National Buoy Data Center (**2019**). "Station PCGT2-8779748—South Padre Island CGS, TX," https://www.ndbc.noaa.gov (Last viewed 12/16/2019).

Nightingale, K. R., Nightingale, R. W., Palmeri, M. L., and Trahey, G. E. (**2000**). "A finite element model of remote palpation of breast lesions

using radiation force: Factors affecting tissue displacement," Ultrason. Imag. **22**(1), 35–54.
Orth, R. J., Carruthers, T. J. B., Dennison, W. C., Duarte, C. M., Fourqurean, J. W., Heck, K. L., Hughes, A. R., Kendrick, G. A., Kenworthy, W. J., Olyarnik, S., Short, F. T., Waycott, M., and Williams, S. L. (**2006**). "A global crisis for seagrass ecosystems," BioScience **56**(12), 987–996.
Prosperetti, A., Crum, L. A., and Commander, K. W. (**1988**). "Nonlinear bubble dynamics," J. Acoust. Soc. Am. **83**(2), 502–514.
Roberts, D. G., and Caperon, J. (**1986**). "Lacunar gas discharge as a measure of photosynthesis in seagrasses," Mar. Ecol. **29**, 23–27.
Sagers, J. D., and Knobles, D. P. (**2014**). "Statistical inference of seabed sound-speed structure in the Gulf of Oman Basin," J. Acoust. Soc. Am. **135**(6), 3327–3337.
Sen, M. K., and Stoffa, P. L. (**1995**). *Global Optimization Methods in Geophysical Inversion* (Elsevier, Amsterdam).
Short, F., Carruthers, T., Dennison, W., and Waycott, M. (**2007**). "Global seagrass distribution and diversity: A bioregional model," J. Exp. Mar. Biol. Ecol. **350**(1), 3–20.
Silva, J., Sharon, Y., Santos, R., and Beer, S. (**2009**). "Measuring seagrass photosynthesis: Methods and applications," Aquatic Biol. **7**, 127–141.
Song, J., Bai, J., and Zhou, Y. (**2016**). "Intraluminal bubble dynamics induced by lithotripsy shock wave," J. Phys. D **49**, 485401.
Spratt, K. S., Hamilton, M. F., Lee, K. M., and Wilson, P. S. (**2017**). "Radiation damping of, and scattering from, an arbitrarily shaped bubble," J. Acoust. Soc. Am. **142**(1), 160–166.
Tarantola, A. (**2005**). *Inverse Problem Theory and Methods for Model Parameter Estimation* (Siam, Philadelphia, PA), Chap. 3.
Wan, L., Badiey, M., Knobles, D. P., and Wilson, P. S. (**2018**). "The airy phase of explosive sounds in shallow water," J. Acoust. Soc. Am. **143**(3), EL199–EL205.
Waycott, M., Duarte, C. M., Carruthers, T. J. B., Orth, R. J., Dennison, W. C., Olyarnik, S., Calladine, A., Fourqurean, J. W., Heck, K. L., Hughes, A. R., Kendrick, G. A., Kenworthy, W. J., Short, F. T., and Williams, S. L. (**2009**). "Accelerating loss of seagrasses across the globe threatens coastal ecosystems," Proc. Natl. Acad. Sci. **106**(30), 12377–12381.
Westwood, E. K., Tindle, C. T., and Chapman, N. R. (**1996**). "A normal mode model for acousto-elastic ocean environments," J. Acoust. Soc. Am. **100**(6), 3631–3645.
Wilson, P. S., and Dunton, K. H. (**2009**). "Laboratory investigation of the acoustic response of seagrass tissue in the frequency band 0.5–2.5 kHz," J. Acoust. Soc. Am. **125**(4), 1951–1959.
Wilson, P. S., Ellzey, J. L., and Muir, T. G. (**1995**). "Experimental investigation of the combustive sound source," IEEE J. Oceanic Eng. **20**(4), 311–320.
Wilson, C. J., Wilson, P. S., and Dunton, K. H. (**2012**). "An acoustic investigation of seagrass photosynthesis," Mar. Biol. **159**(10), 2311–2322.
Wilson, C. J., Wilson, P. S., Greene, C. A., and Dunton, K. H. (**2010**). "Seagrass leaves in 3-D: Using computed tomography and low-frequency acoustics to investigate the material properties of seagrass tissue," J. Exp. Mar. Biol. Ecol. **395**, 128–134.
Wood, A. B. (**1946**). *A Textbook of Sound*, 2nd ed. (Bell, London).